



Eulerian and Lagrangian views of warm and moist air intrusions into summer Arctic

Cheng You^{a,*}, Michael Tjernström^a, Abhay Devasthale^b

^a Department of Meteorology & Bolin Centre for Climate Research, Stockholm University, Stockholm, Sweden

^b Remote Sensing Unit, Research and Development Department, Swedish Meteorological and Hydrological Institute, Norrköping, Sweden

ARTICLE INFO

Keywords:

Arctic climate
Boundary-layer
Warm and moist air intrusion
Trajectories

ABSTRACT

In this study, warm and moist air intrusions (WaMAI) over the sea sectors of Kara, Laptev, East Siberian and Beaufort from 1979 to 2018 are identified in ERA5 reanalysis and their air-mass transformation is analysed using interpolation in ERA5 and satellite products along trajectories. The analysis shows that WaMAIs, driven by blocking high-pressure systems over the respective ocean sectors, induce surface warming ($11\text{--}18\text{ W m}^{-2}$) and sea ice melt from positive anomalies of net longwave radiation ($5\text{--}8\text{ W m}^{-2}$) and turbulent flux ($8\text{--}13\text{ W m}^{-2}$) to the surface, although the anomaly of net shortwave radiation ($-9\text{--}+1\text{ W m}^{-2}$) is negative. From a Lagrangian perspective, the surface energy-budget anomaly decreases linearly, while total column cloud liquid water (TCLW) increases linearly with the downstream distance from the sea-ice edge. However, the cloud radiative effects of both longwave and shortwave radiation reach an equilibrium as TCLW increases in a much lower rate beyond 7 degrees north of the sea ice edge. The boundary-layer energy-budget pattern can be categorized into two classes: radiation-dominated and turbulence-dominated, comprised of 26% and 62% WaMAIs respectively. Statistically, turbulence-dominated cases occur with 3 times stronger large-scale subsidence, and also feature a larger anomaly in net shortwave radiation. In radiation-dominated WaMAIs, stratocumulus develops more strongly and hence exerts larger longwave and shortwave forcing to the surface. In both categories, a well-mixed boundary layer deepens by 500 m along the trajectories, from the continuous turbulent mixing.

1. Introduction

Arctic near-surface temperatures have increased more than twice as fast as the global average in recent decades (Cohen et al., 2014; Francis and Vavrus, 2012; Graversen et al., 2008). This phenomenon, known as Arctic amplification (AA; Serreze and Francis, 2006), has contributed to dramatic melting of Arctic sea ice (Simmonds, 2015), rapid decline of spring snow cover (Derksen and Brown, 2012), thawing of permafrost (Lawrence et al., 2008) and continued retreat of Greenland's ice sheet (Tedesco et al., 2013). Although many of the individual processes

contributing to Arctic amplification are understood, their relative importance and interactions are poorly known (Vihma et al., 2014).

Several previous studies suggested that warm-and-moist-air intrusions (WaMAI) into the Arctic from southerly latitudes significantly contribute to AA (Woods and Caballero, 2016; Johansson et al., 2017; Liu et al., 2018; Messori et al., 2018; Naakka et al., 2019). Woods et al. (2013) found that the positive trend in number of WaMAIs episodes can statistically explain a substantial part of the surface-air temperature and sea-ice concentration trends in the Barents Sea (Woods and Caballero, 2016). Kapsch et al. (2013, 2016) linked additional incoming longwave

Abbreviations: AA, Arctic Amplification; AIRS, Atmospheric Infrared Sounder; CERES, Clouds and the Earth's Radiant Energy System; CRE, Cloud Radiative Effects; DIN, Double inversion; EMIs, Extreme moisture intrusions; F_{lw} , Surface net longwave irradiance; $F_{\text{lw}}^{\text{CRE}}$, CRE on F_{lw} ; $F_{\text{lw}}^{\text{CRE,CERES}}$, CRE on F_{lw} from CERES products; F_{sh} , Surface turbulent latent heat fluxes; F_{sh} , Surface turbulent sensible heat fluxes; F_{net} , Surface net shortwave irradiance; $F_{\text{net}}^{\text{CRE}}$, CRE on F_{net} ; $F_{\text{net}}^{\text{CRE,CERES}}$, CRE on F_{net} from CERES products; F_{total} , Total surface energy budget; F_{sh} , F_{sh} + F_{net} ; f_{net} , Vertically integrated northward water vapor flux; GH_{500} , 500-hPa geopotential height; h_{lw} , the heights to the maximum longwave cooling; h_{sh} , the heights to the maximum specific humidity; h_{net} , the heights to the maximum turbulent cooling; h_{net} , the heights to the maximum turbulent warming; h_{v} , the height to the maximum vertical temperature gradient; RAD, Radiation dominated energy-budget category; SIC, Sea ice concentration; SYN, Synoptic TOA and surface fluxes and clouds; T_{min} , 2 m temperature; T_{850} , 850-hPa temperature; TBL, Turbulence dominated energy-budget category; T&R, TBL and RAD; TCLW, Total column cloud liquid water; T_s , Surface temperature; WaMAIs, Warm and moist air intrusions.

* Corresponding author.

E-mail address: cheng.you@misu.su.se (C. You).

<https://doi.org/10.1016/j.atmosres.2021.105586>

Received 3 November 2020; Received in revised form 3 February 2021; Accepted 18 March 2021

Available online 20 March 2021

0169-8095/© 2021 The Author(s). Published by Elsevier B.V. This is an open access article under the CC BY license (<http://creativecommons.org/licenses/by/4.0/>).

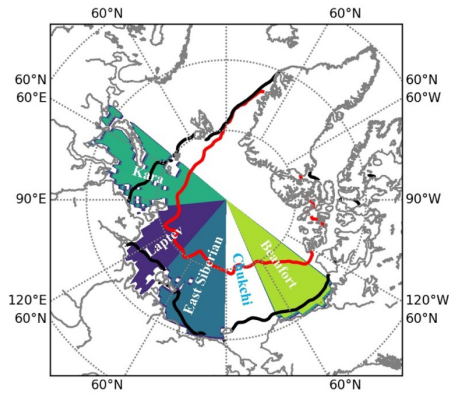


Fig. 1. Locations of four sea sectors discussed in this paper, the Kara, Laptev, East Siberian and Beaufort Sea sectors. Black line is the mean September sea-ice edge of 1979–2018 and red line is the mean September sea-ice edge in 2012 when the minimum sea-ice cover was recorded.

surface radiation to an earlier sea-ice melt onset and hence a lower September ice extent. Climatologically, cloudiness increased by 30% during Arctic warm-air intrusions and hence additional radiative heating (up to 0.15 K/d) was exerted on the atmosphere (Johansson et al., 2017).

Most previous studies focus on winter WaMAIs, although we have the least observational evidence in winter. With no or little solar

radiation in winter, the analysis of cloud effects on radiative transfer during WaMAIs is simplified. Summer WaMAIs, however, have another particular feature of interest. As soon as the surface melt has started and as long as an appreciable amount of ice or snow is left on the surface, the surface temperature is prohibited from rising above the melting point by the latent heat of the phase change, regardless of the air temperature aloft. This creates a special surface-boundary condition for air-mass transformation that exists only in summer. At the same time, the competing effects from cloud formation, with attenuation of solar radiation and enhanced longwave radiation at the surface, complicates the analysis (e.g. Tjernström et al., 2019a).

Most studies were conducted from an Eulerian perspective, retrieving composite mean of WaMAIs properties (Liu et al., 2018), or calculating regressions between different metrics (Gong and Luo, 2017). Based on observations of a particularly strong summer WaMAI event, Tjernström et al., 2015, 2019b argued the need to understand the physical processes that leads to the warming effect of summer WaMAIs, and hence to study the air mass transformation linking summer WaMAIs to Arctic warming and sea-ice decrease. Both Pithan et al. (2018) and Komatsu et al. (2018) suggested a Lagrangian approach on WaMAI research. You et al. (2020) designed a method where trajectories are used in combination with satellite observations and reanalysis to analyze WaMAIs in a Lagrangian perspective and also tested this method on the event described in Tjernström et al. (2015). Here we will extend this to build a climatology of effects by summer WaMAIs, in terms of the boundary-layer structure and the energy-budgets for both atmospheric boundary layer and the sea ice surface.

2. Method

2.1. Data

The detection and Eulerian analysis of WaMAIs is primarily based on

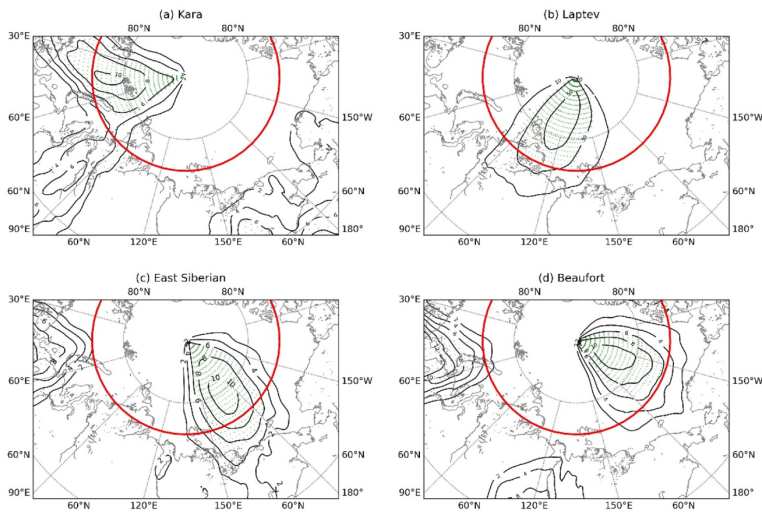


Fig. 2. Contours of the correlation between local f_w and SIC anomalies (multiplied by -1) for the summer month (JJA) in (a) Kara, (b) Laptev, (c) East Siberian and (d) Beaufort Sea. The stippling indicates statistical significance at the $p < 0.05$ level for the Student's t -test. Red line is the latitude of 75°N where the trajectories are launched.

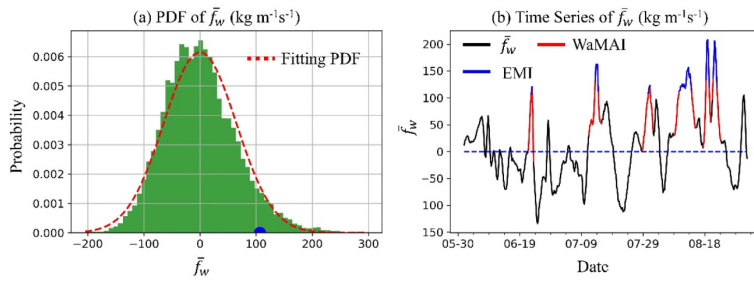


Fig. 3. For summer (JJA) 1983 as an example, (a) shows the Probability Distribution Function of \bar{f}_w (kg m⁻¹ s⁻¹), with the 95-percentile marked as a blue dot, and (b) the time series of \bar{f}_w with WaMAI highlighted in red and EMIs highlighted in blue.

data from the European Centre for Medium-Range Weather Forecast (ECMWF) latest reanalysis, ERA5 (Hersbach et al., 2020) over the period of June–August from 1979 to 2018, with a 6-hourly temporal resolution and a 0.75° horizontal resolution. This includes the vertically integrated northward water vapor flux (f_w), sea ice concentration (SIC), 500-hPa geopotential height (GH₅₀₀), 2 m air temperature (T_{2m}), 850-hPa temperature (T_{850}), and total column cloud liquid water (TCLW).

We also use such satellite products as surface radiation flux extracted from the Synoptic TOA and surface fluxes and clouds (SYN), 3-hourly level 3 product (Rutan et al., 2015) from the Clouds and the Earth's Radiant Energy System (CERES) satellite. It is on a 1° × 1° resolution

grid and cover the period over the period of June–August from 2000 to 2018. Surface temperature (T_s) that comes from the Standard Atmospheric Infrared Sounder (AIRS) version 6, level 3 daily pan-Arctic satellite product (Chahine et al., 2006; Devasthale et al., 2016; Susskind et al., 2014) is also utilized. It is on a 1° × 1° resolution grid and cover the period of June–August from 2003 to 2018. Moreover, we also use satellite-observed daily sea ice concentration (SIC) from the National Snow and Ice Data Center (NSIDC).

For the Lagrangian analysis of WaMAIs, we use the same datasets but at a higher temporal resolution. This includes 1-hourly surface net solar irradiance (F_{sw}) and surface net thermal irradiance (F_{lw}) from both ERA5

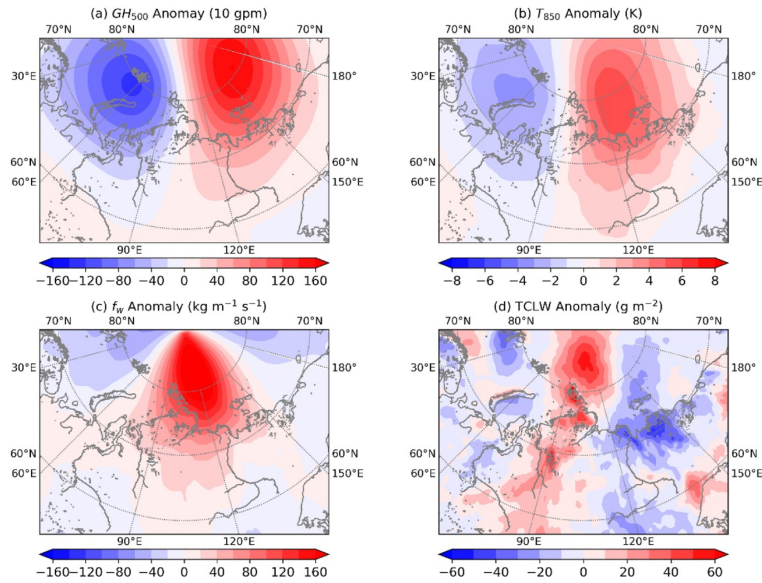


Fig. 4. Composite ERA5 anomalies of (a) 500-hPa GH (10 gpm), (b) 850-hPa temperature (K), (c) northward water-vapor flux (kg m⁻¹ s⁻¹), total column cloud liquid water (g m⁻²), for all EMIs during 1979–2018 summers.

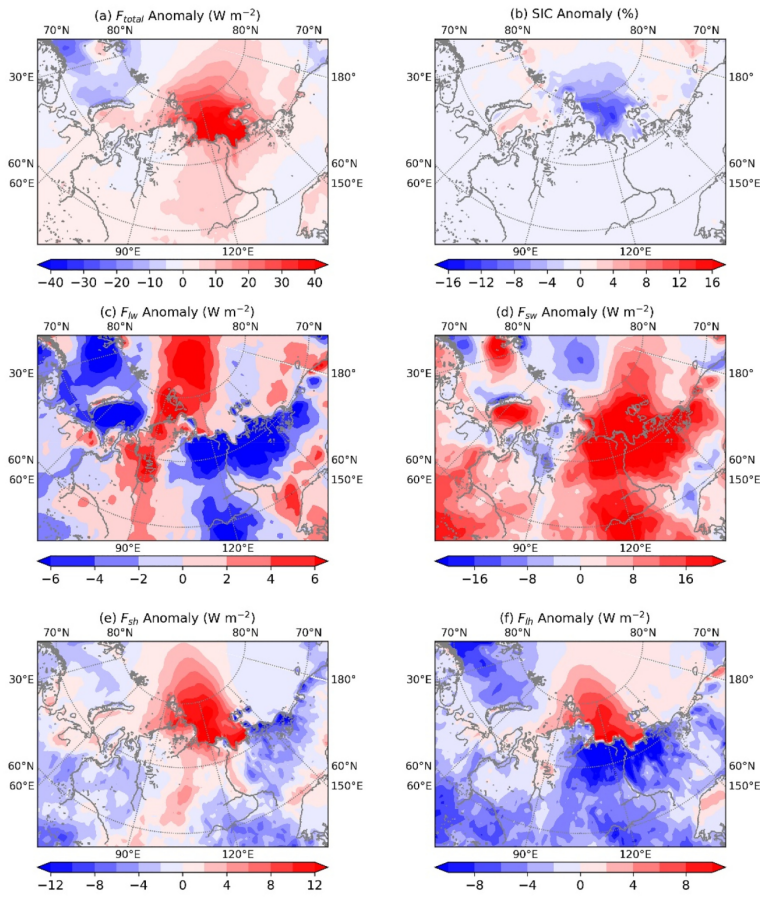


Fig. 5. Composite ERA5 anomalies of (a) total surface energy (W m^{-2}), (b) sea ice concentration (%), (c) surface thermal net radiative flux (W m^{-2}), (d) surface net solar radiative flux (W m^{-2}), (e) surface sensible heat flux (W m^{-2}) and (f) surface latent heat flux (W m^{-2}) for all EMIs during 1979–2018 summer.

and SYN. It also includes surface sensible heat flux (F_{sh}) and surface latent heat flux (F_{lh}) from ERA5, as well as 1-hourly temperature tendencies due to different model physics at model levels from ERA5.

Relying on reanalysis especially for the energy budget terms introduces uncertainty. Mean variables are constrained in reanalysis by assimilating observations in the data assimilation. However, in-situ observations over the central Arctic Ocean are sparse, except for during some field campaigns and polar orbiting satellites are plentiful due to the geometry of satellite orbits (Tjernström et al., 2019a). In a systematic study of observation impact on analysis and forecasting, Lawrence et al. (2019) concluded that both in-situ and satellites are important, with a slight additional weight to satellite observations in summer and in-situ conventional observations in winter. The latter is presumably because of the loss of all visible wavelengths in passive

remote sensing in winter.

Several limited evaluations of different reanalysis (e.g. De Boer et al., 2014; Graham et al., 2019a, 2019b; Jakobson et al., 2012; Wesslén et al., 2014) or of related models (Sotiropoulou et al., 2016; Tjernström et al., 2020) show that they all suffer from systematic errors, especially for parameters that have roots in the model's sub-grid parameterizations. Moreover, these errors are typically seasonally dependent. However, it is not possible to climatologically analyze air mass transformation on energy budgets or clouds along a trajectory with any other ways than using reanalysis.

The strength of reanalysis is that it combines observed states with an internally consistent numerical model. If there are errors, and there is, they are errors in individual processes, and there likely is, they at least compensating. In this study we alleviate the uncertainty in two ways;

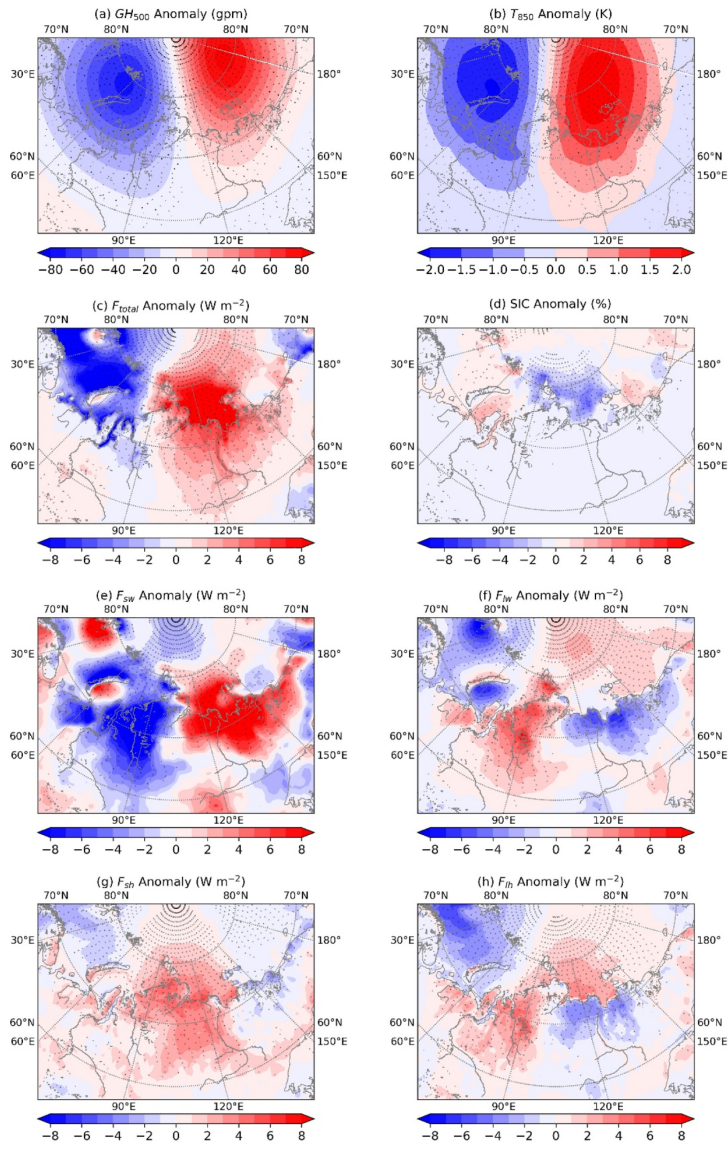


Fig. 6. Anomalies of (a) 500-hPa geopotential height (gpm), (b) 850-hPa temperature (K), (c) F_{total} , (d) SIC, (e) F_{sw} , (f) F_{net} , (g) F_{gh} , and (h) F_g from linear regressions against daily \bar{f}_w time series in the Laptev Sea. The stippling indicates statistical significance at the $p < 0.05$ level from a Student's t -test.

Table 1

Regional averaged F_{sh} , F_{lh} , F_{sw} , F_{lw} and F_{total} in Kara, Laptev, East Siberian and Beaufort Sea sector. The unit is $W m^{-2}$ for all variables.

Sea sector	Kara	Laptev	East Siberian	Beaufort
F_{sh}	7.47±5.6	7.12±6.0	5.26±5.6	4.52±5.2
F_{lh}	6.14±5.3	4.15±6.0	4.94±5.6	4.04±6.2
F_{sw}	-9.57±35.0	-2.10±33.7	1.46±45.0	-4.79±32.4
F_{lw}	8.66±9.4	5.75±8.5	6.51±7.4	7.65±6.9
F_{total}	12.7±31.5	14.92±31.4	18.17±41.0	11.42±29.5

first, by averaging over a large number of cases and second by considering anomalies rather than actual mean values. Avoiding single case reduces random errors, while considering anomalies reduces systematic errors. Additionally, we also compare reanalysis results with corresponding satellite products.

2.2. WaMAI detection

We use f_w to detect WaMAIs, over the sea sectors of Kara, Laptev, East Siberian and Beaufort separately (Fig. 1). Other important sectors, like the Barents and Chukchi Seas, are omitted. In the Barents Sea, it is almost ice free in summer, while in the Chukchi Sea, we find that the variation of the sea ice is significantly related statistically to WaMAIs over the East Siberian Sea.

Fig. 2 shows the local regression between the summer (JJA) anomalies of f_w and SIC (multiplied by -1) for the Kara, Laptev, East Siberian and Beaufort Seas. For all these basins we see that large f_w is associated with a strong SIC decrease. Locations where a Student's *t*-test indicate significance >95% are considered sensitive regions. The average f_w over each sensitive region, \bar{f}_w , is approximately normally distributed; as an example, we show the probability distribution of \bar{f}_w for the Laptev Sea in Fig. 3a. Here the cases when $\bar{f}_w > 0$ and a maximum larger than the 95-percentile are considered WaMAIs. Portions of a WaMAI larger than the 95-percentile are considered extreme intrusions, EMIs (Fig. 3b).

Two days forward and backward trajectories are calculated for each WaMAI event in each ocean basin using the algorithm from Woods et al. (2013). Launch points at 75°N are set to the location where T_{850} is the largest while the terminal points of each forward (backward) trajectory is defined as where a trajectory starts tracking southward (northward). Hence, we only capture the part of each trajectory that continuously tracks northward. Therefore, as a trajectory crosses the pole, it by definition starts southward and the pole is then the terminal point. In reality, most trajectories bend southward much earlier, and then the terminal point is their northernmost point. Finally, selected trajectories have to conform to two additional criteria: 1) the terminal point has to be located north of 80°N and at least 5° north of the sea-ice edge, defined as where temperature gradient over the sea is maximum; 2) the northernmost location of 5 °C temperature-contour should be at least 5° north of the sea-ice edge. Eventually, 42, 63, 62 and 67 WaMAIs are detected over the sea sectors of Kara, Laptev, East Siberian and Beaufort, respectively, for a total of 234 during the summer months over the 40 years, roughly consistent with the statistics in Sedlar and Tjernström (2017). The launch time and longitude of these 234 trajectories are listed in Table A1. Trajectory calculation is also prone to uncertainty (Bowman et al., 2013). Trajectories rely only on the resolved-scale motions that here come from reanalysis which is uncertain to begin with. Additional uncertainty also comes from interpolation errors in the gridded wind fields from the reanalysis. The uncertainty grows with the length of the trajectories and with the temporal and spatial resolution of the wind fields. Restricting the trajectories to two days and using ERA5

with 6-hourly output and reasonably good spatial resolution should reduce the error to within O(10 km), see Bowman et al. (2013). A Lagrangian study of air-mass transformation in the boundary layer using trajectories strictly only works in barotropic flow, where the wind varies little with height. However, such ideal conditions rarely exist and a compromise is necessary.

Following You et al. (2020), trajectories are calculated at several different heights, every 100 m, from 300 m to 800 m. Vertical profiles of the various variables are then extracted from reanalysis, from the surface to 2 km, by interpolation in time and space along each of these trajectories. The final vertical cross-section for each WaMAI is the ensemble average of the result for all trajectories.

2.3. Energy budgets

The surface energy budget can be written as

$$F_{total} = F_{sw} + F_{lw} + F_{sh} + F_{lh} \quad (1)$$

where F_{sw} and F_{lw} are surface net solar and thermal irradiance, and F_{sh} and F_{lh} are the surface turbulent sensible and latent heat fluxes, respectively. Note that all surface net energy fluxes are considered positive when contributing to a surface warming; ocean heat fluxes are not considered here. Individual terms in Eq. 1 are also interpolated from ERA5 at each 0.5-degree interval in latitude along the trajectories. With the same method, we also look at the cloud radiative effects (CRE) on F_{sw} ($F_{sw,CRE}$) and F_{lw} ($F_{lw,CRE}$). They are defined by.

$$F_{sw,CRE} = F_{sw,all_sky} - F_{sw,clear_sky}, F_{lw,CRE} = F_{lw,all_sky} - F_{lw,clear_sky} \quad (2)$$

In Eq. 2, F_{sw,all_sky} and F_{lw,all_sky} are the surface net solar and thermal irradiances, considering the actual clouds present, while $F_{sw,clear_sky}$ and $F_{lw,clear_sky}$ are clear-sky counterparts, assuming clouds were not present even if there was.

To explore the boundary-layer energy budget, we also extract temperature tendencies due to different model physics from ERA5, with which we can resolve all terms in the thermal equation

$$T_t = \frac{\partial T}{\partial t}_{sw} + \frac{\partial T}{\partial t}_{lw} + \frac{\partial T}{\partial t}_{LH} + \frac{\partial T}{\partial t}_{TH} \quad (3)$$

Here, temperature tendency T_t of an air-mass in a WaMAI is due to heating/cooling from shortwave irradiance ($\frac{\partial T}{\partial t}_{sw}$), longwave irradiance ($\frac{\partial T}{\partial t}_{lw}$), latent heat of condensation in cloud formation ($\frac{\partial T}{\partial t}_{LH}$), and vertical turbulent heat transport ($\frac{\partial T}{\partial t}_{TH}$). Note that in a Lagrangian sense, the advection tendencies are by definition zero, while in a Eulerian sense they would additionally be balanced by temperature advection. All these terms are also interpolated along the trajectories as previously discussed.

3. Results

3.1. Large-scale features

We identified EMIs for the Arctic ocean basins of Kara, Laptev, East Siberian and Beaufort. As an example, Fig. 4 shows a composite of all EMIs over the Laptev Sea. The composite of the GH₅₀₀ anomaly (Fig. 4a) shows a strong dipole anomaly, producing an intensive f_w anomaly into the Arctic (Fig. 4c), which is consistent with an anticyclonic circulation, during strong WaMAI episodes found in previous studies (Tjernström et al., 2015; Overland and Wang, 2016; Gong and Luo, 2017; Johansson et al., 2017; Sedlar and Tjernström, 2017; Messori et al., 2018; Cox et al., 2019). The enhanced temperature advection and cloud formation are

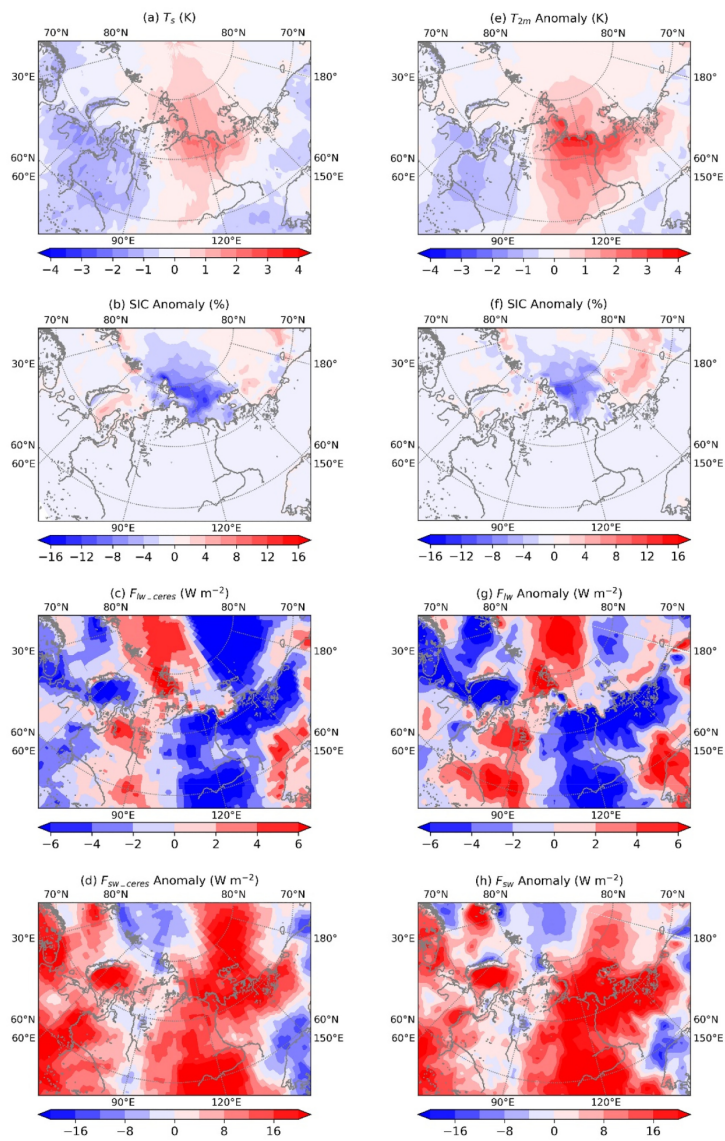


Fig. 7. Composite of anomalies in (a) AIRS surface temperature (K), (b) NSIDC sea-ice concentration (%), (c) net surface longwave and (d) shortwave irradiance (both in $W m^{-2}$). Figures e-h are their counterparts from ERA5 reanalysis.

Table 2

Regional averaged F_{net} , F_{lw} and their counterparts from CERES in Kara, Laptev, East Siberian and Beaufort Sea sector. The unit is W m^{-2} for all variables.

Sea sector	Kara	Laptev	East Siberian	Beaufort
$F_{\text{net, CERES}}$	-9.09 ± 33.8	0.012 ± 39.6	3.96 ± 58.0	-4.19 ± 43.0
F_{lw}	-11.35 ± 29.9	-3.58 ± 32.1	-0.82 ± 44.0	-6.02 ± 32.9
$F_{\text{net, CERES}}$	6.76 ± 6.3	1.40 ± 8.1	2.81 ± 8.0	4.91 ± 8.3
F_{lw}	9.35 ± 8.7	5.29 ± 9.0	6.27 ± 7.5	7.43 ± 6.9
$F_{\text{net, CERES}} + \text{ice, CERES}$	-2.33 ± 33.0	1.41 ± 37.4	6.77 ± 56.8	0.72 ± 41.5
$F_{\text{net, lw}}$	-2.0 ± 26.4	1.71 ± 29.5	5.45 ± 42.4	1.41 ± 31.2

manifested by the positive T_{850} and TCLW anomalies in Fig. 4c and d, respectively. These features in the GH₅₀₀, T_{850} and TCLW anomalies are also found in all the other three ocean basins.

As warm and moist air is advected into the Arctic, it interacts with the cool surface through turbulence and radiation, enforcing positive F_{sh} and F_{lh} anomalies at the surface (Fig. 5e and f). The F_{sh} anomaly reaches $\sim 10 \text{ W m}^{-2}$ at the coast, tapering off northward all the way to the pole. The pattern of F_{lh} anomaly is similar to that of F_{sh} but the magnitude is somewhat smaller. The long and narrow belt of TCLW anomaly in Fig. 4d, extending from 60°N to the north pole along the path of the EMIs, affects the surface energy-budget by enhancing F_{lw} and attenuating F_{sw} on the surface, respectively (Fig. 6e and f). The anomalies sum up to a positive F_{total} anomaly, inducing decreased SIC (Fig. 5b). Note that the SIC decrease could also be contributed by sea-ice drift. This surface energy-budget setting agrees well with the in situ observations from an EMI in the East Siberian Sea during a field campaign on the icebreaker Oden (Tjernström et al., 2015, 2019b). Similar relation between F_{lw} anomaly and winter EMIs is also found in other climatological analysis (Gong et al., 2017; Gong and Luo, 2017).

From averaged surface-energy budgets over sea ice in the sensitive regions across the four basins (Table 1, Fig. 2), a complex picture emerges. Except for in the Laptev Sea, F_{lw} anomalies are larger than those for the turbulent heat fluxes. However, since F_{lh} and F_{sw} anomalies typically have opposite signs, the cloud-effects on the surface energy-budget tend to partly offset, leaving the turbulent flux anomalies to dominate F_{total} . These results are consistent with the conclusions from Tjernström et al. (2019b), compiling surface energy-budget observations from the summer of 2014 along the Russian coast, comparing on- and off-ice flows. During the particularly strong WaMAI analysed in Tjernström et al. (2015), the observed estimated F_{total} anomaly was -15 W m^{-2} , consistent with the results in Table 1. Due to a strong sensitivity to cloud properties, the variability in F_{total} is dominated by F_{sw} ; this will be discussed further in section 3.2.

Fig. 5 shows the spatial distribution of the surface energy-budget anomalies for EMIs over the Laptev Sea. The maxima of the turbulent heat-flux anomalies and the net anomaly are located near the coast,

gradually decreasing as the warm-air is advected farther into the high Arctic, reflecting the air-mass transformation. The main positive F_{lw} and negative F_{sw} anomalies are more evenly distributed over the latitudes. Also note that irradiance anomalies have opposite sign on the eastern flank of the EMIs, where high-pressure center is located and hence clouds tend to dissipate (negative TCLW anomaly in Fig. 4d).

The composites of large-scale pattern discussed above are extracted from extreme events which may not necessarily represent the general pattern of all WaMAIs. Therefore, linear regressions of GH, T_{850} , SIC, F_{total} , F_{sh} , F_{lh} , F_{sw} and F_{lw} anomalies against the time series of daily averaged \bar{f}_w are calculated for all the examined ocean basins; the Kara, Laptev, East Siberian and Beaufort Seas. Since the regressions over these four regions lead to the same conclusion, the Laptev Sea is again taken as an example (Fig. 6). All the regressed fields have similar pattern as their counterparts in Figs. 4 and 5, implying a similar relationship for all WaMAIs but at smaller magnitudes.

We also compare the anomalies of T_{2m} , SIC, F_{lw} and F_{sw} from ERA5 with their counterparts from corresponding satellite products (Fig. 7) as a sanity check. The T_{2m} anomaly from ERA5 has a similar pattern and magnitude as the T_s anomaly from AIRS over the ocean, but the T_{2m} anomaly over land is much larger than that of T_s (Fig. 7a, e). They also share similar pattern and magnitude for the SIC anomaly, but in ERA5 the maximum SIC values are shifted north compared to that from NSIDC (Fig. 7b, f). The F_{lw} and F_{sw} anomalies from ERA5 also share similar patterns and magnitudes with those from CERES, except larger distinction in the Arctic (Fig. 7c, f; Fig. 7d, g), implying that the ERA5 reanalysis has stronger cloud effects in the Arctic by inducing weaker shortwave forcing but stronger longwave forcing on the surface (Table 2). In CERES, the enhanced longwave forcing mostly offsets the enhanced negative shortwave forcing and hence the total surface radiative forcing is similar to that in ERA5 even if the individual terms are larger (Table 2). Stengel et al. (2018) also found this Arctic cloud overestimation in ERA-interim reanalysis, consistent with cloud problems in the ECMWF Integrated Forecasting System, the atmospheric model powering the ERA5 reanalysis dataset (Tjernström et al., 2020). Although details might differ, the large agreements between ERA5 and satellite products give us confidences to conduct Lagrangian analyses with ERA5 dataset in following sections.

3.2. The surface energy-budget

As the warm-air propagates over the sea ice, a large temperature gradient is formed in the vertical. From 0 to 7 degrees north of the sea ice edge, the height to the maximum vertical temperature gradient (h_{tg}) and TCLW increase almost linearly by 50 m degree^{-1} and $17 \text{ g m}^{-2} \text{ degree}^{-1}$, respectively, implying that stratocumulus develop intensively during this period (Fig. 8). Afterwards, they increase at a much slower rate. The

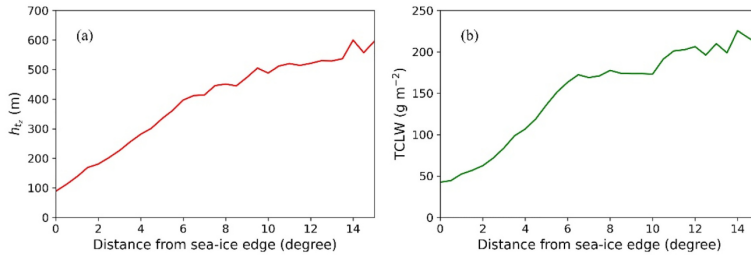


Fig. 8. Average variation of (a) the height to the maximum temperature gradient (m) and (b) total column cloud liquid water (g m^{-2}) with the downstream northward distance from sea-ice edge, along the WaMAI trajectories. Note that this is not necessarily the distance travelled, since WaMAIs need to travel due northward.

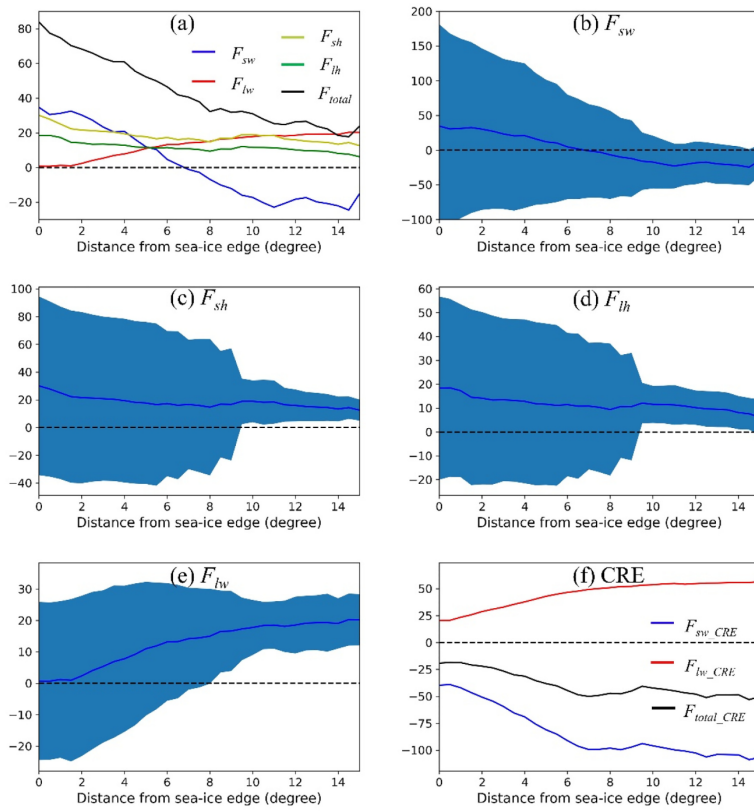


Fig. 9. Plots showing the average meridional change in the anomalies of (a) the sum (F_{total} , $W m^{-2}$; black) and individual surface fluxes of sensible heat (F_{sh} , $W m^{-2}$; yellow), latent heat (F_{lh} , $W m^{-2}$; green), net longwave irradiance (F_{lw} , $W m^{-2}$; red) and net shortwave irradiance (F_{sw} , $W m^{-2}$; blue) along the trajectories. In (b-e) each individual flux anomaly is shown again, including the spread F_{sw} , F_{lh} , F_{lw} and F_{lw} . (f) shows the cloud radiative effect by shortwave (F_{sw_CRE} ; blue), longwave (F_{lw_CRE} ; red) and the total (F_{total_CRE} ; black).

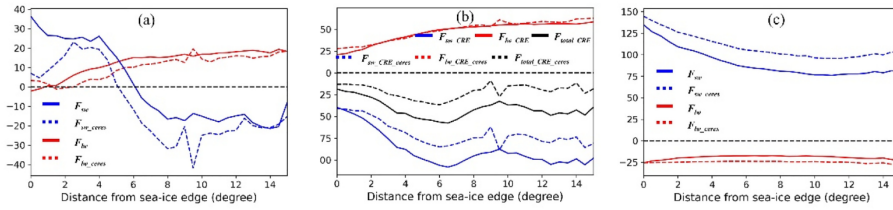


Fig. 10. (a) Average anomalies of net surface longwave (red) and shortwave (blue) irradiance from ERA5 (solid) and CERES (dashed) along the trajectories; (b) cloud radiative effect by shortwave (blue), longwave (red) and total (black) from ERA5 (solid) and CERES (dashed) along the trajectories; (c) climatological mean of net surface longwave (red) and shortwave (blue) irradiance from ERA5 (solid) and CERES (dashed) along the trajectories.

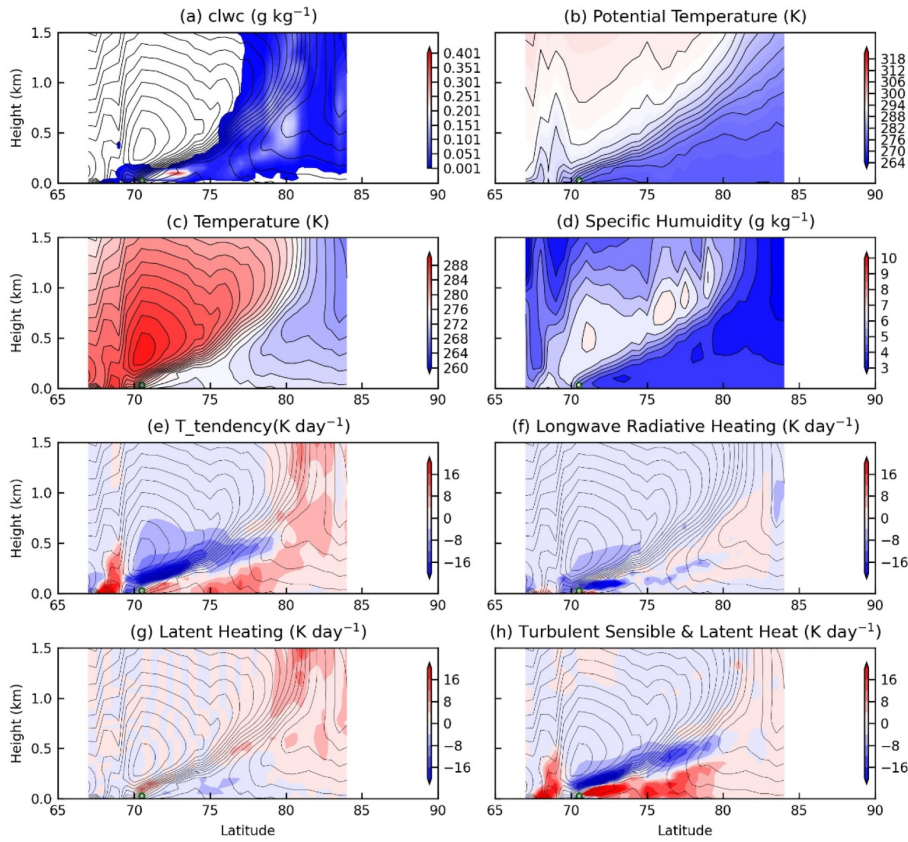


Fig. 11. Latitude-height cross-section of (a) cloud liquid water concentration (g kg^{-1}), (b) potential temperature (K), (c) temperature (K), (d) specific humidity (g kg^{-1}), (e) temperature tendency due to model physics (K day^{-1}), (f) longwave radiative heating (K day^{-1}), (g) latent heating (K day^{-1}) and (h) turbulent heating (K day^{-1}), interpolated from ERA5 along trajectories of one selected turbulent-dominated WaMAL. The green dot in (a) marks the location of ice-edge. See the text for a detailed discussion.

gradual increase of h_{ice} , which is a manifestation of increased boundary-layer mixing, leads to a reduction in near-surface gradients. Since the turbulent heat fluxes at the surface are dependent on these gradients, F_{sh} and F_{lh} anomalies also gradually decrease until 8 degrees north of sea-ice edge (Fig. 9c, d). Farther north, they start to increase slightly but decrease again from 10 degrees north of sea-ice edge till the central Arctic (Fig. 9c, d). The spreads of F_{sh} and F_{lh} are large initially but around 10 degrees north of the ice edge both F_{sh} and F_{lh} anomalies become significantly positive (Fig. 9c, d). Simultaneously, F_{lw} anomaly increases almost linearly by $3 \text{ W m}^{-2} \text{ degree}^{-1}$ from 0 to 7 degrees north of the sea

ice edge, but does not become significantly larger than zero until around ~ 10 degrees into the sea ice (Fig. 9e), while F_{dw} anomaly decreases linearly by $6 \text{ W m}^{-2} \text{ degree}^{-1}$ from 0 to 11 degrees into the sea ice but it never becomes significantly positive or negative (Fig. 9b). The variation of both F_{dw} and F_{lw} along trajectories are due to the cloud radiative effects of the stratocumulus. As shown in Fig. 9f, $F_{\text{sw,CRE}}$ ($F_{\text{lw,CRE}}$) decreases (increases) from 0 to 7 degrees north of sea-ice edge and remain almost unchanged afterwards (Fig. 9f). However, the net effect of CRE is always negative, manifesting that F_{sh} and F_{lh} are the main contributor of surface warming during WaMAL.

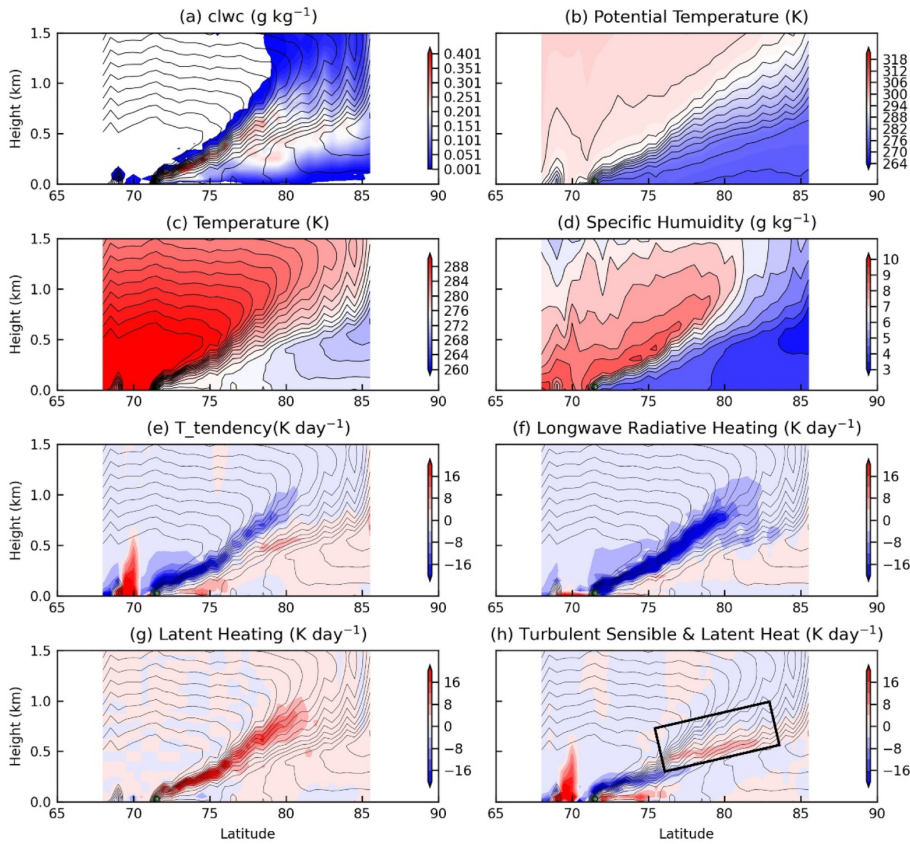


Fig. 12. Same as Fig. 11 but for a selected radiation-dominated WaMAI.

Unlike the larger-scale features in Table 2, both F_{lw} and F_{sw} anomalies, in particular the latter, are larger in ERA5 (Fig. 10a) in comparison with their counterparts from CERES. However, $F_{lw,CRE}$ in ERA5 develops in parallel to its counterpart in CERES ($F_{lw,CRE,CERES}$), while $F_{sw,CRE}$ is stronger than its CERES counterpart (Fig. 10b). Therefore, the smaller F_{sw} anomaly indicates smaller climatological mean of F_{sw} in ERA5, which implies that climatologically ERA5 overestimates CRE (Fig. 10c). The net CRE in both ERA5 and CERES are negative along the whole way to the central Arctic but is stronger in ERA5 than in CERES (Fig. 10b).

3.3. The boundary-layer energy-budget

As discussed in previous section, cloud formation as part of the air-mass transmission can exert large variability on the surface forcing. Here, we focus on the cloud effects on the boundary-layer energy-budget. For each WaMAI, the boundary-layer energy-budget terms are evaluated and interpolated along the trajectory as described in section 2.

We then analyze the energy-budgets on a case-by-case basis and categorize their patterns into two main categories: a) turbulence-dominated (TBL) and; b) radiation-dominated (RAD). Some typical cases of both categories are shown in Fig. 11–14. To further clarify the two energy-budget patterns for all the four ocean basins, the heights to the maximum longwave cooling (h_{lw}) and to the maximum turbulent cooling and warming (h_{tc} and h_{tw}) in relation to the h_{tc} are illustrated in Fig. 15.

3.4. Turbulence-dominated

About 62% of WaMAIs feature turbulence-dominated (category TBL) energy-budget patterns in the boundary layer (Table 3). For this category, turbulent heating and cooling dominate the boundary-layer energy-budget (Fig. 11e and h), even though stratocumulus develops along the trajectory (Fig. 11a) and affects the radiative processes. Note that the total temperature tendency (Fig. 11e) is balanced by the tendency from advection (not shown) as was illustrated in You et al. (2020). Also note

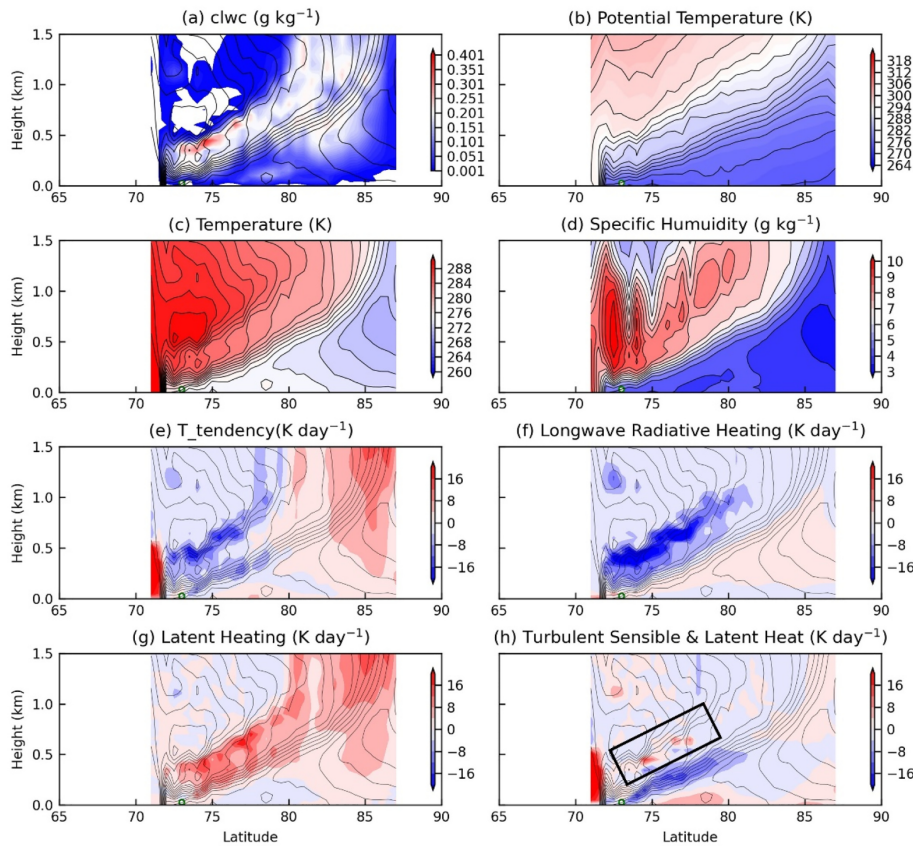


Fig. 13. Same as Fig. 11 but for radiation-dominated WaMAI with double inversions.

that unlike radiation, turbulence does not generate heat by itself. Instead, it heats/cools air locally by redistributing heat from one altitude to another through mixing within the column. As the development of these clouds are considerably suppressed, the cloud water concentrations are usually low (Table 4, TCLW) and the cloud tops are usually located just below the inversion. Consequently, the contribution to the temperature tendency by latent heat release (Fig. 11g) is also small. Turbulent mixing happens across the inversion between the cold surface and the warm air aloft (Fig. 11h). This is also borne out statistically in Fig. 15c, with h_{lc} located near h_{te} and h_{lw} located below h_{lc} . Since the turbulent mixing persists along the trajectories, the well-mixed layer below the inversion is continuously deepened along the trajectory

(Fig. 11b), while the inversion (Fig. 8) and the cloud top are gradually elevated (Fig. 11a). This supports the hypothesis from Tjernström et al. (2019b), that the surface inversion formed at the sea ice edge is eroded progressively downstream, by the entrainment mixing along with the surface turbulent mixing, and eventually the boundary layer must transform into the often observed well-mixed cloud-capped boundary layer (e.g. Tjernström et al. 2012; Sotiropoulou et al., 2014; Brooks et al., 2017).

In this category, stratocumulus develops less strongly than that in category RAD, because of the stronger large-scale subsidence. In most cases from category TBL, large-scale convergence persists along the trajectory (Table 4, CONV), which decreases moisture supply to

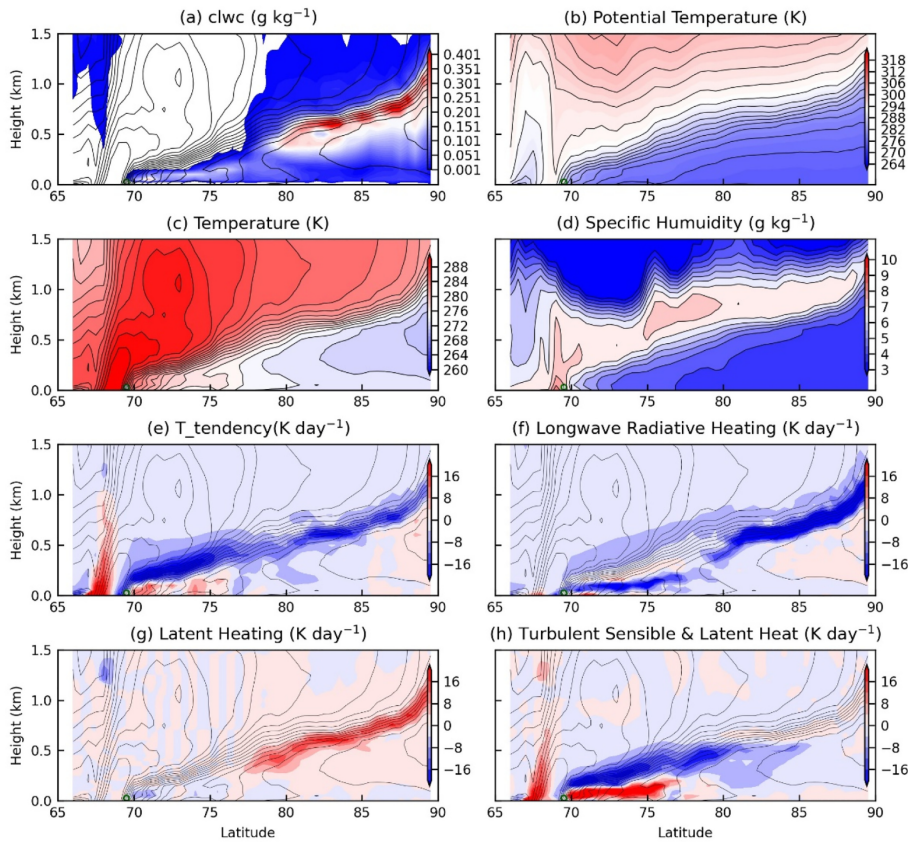


Fig. 14. Same as Fig. 11 but for WaMAI with both turbulence-dominated and radiative-dominated segments.

stratocumulus by entrainment and shorten its lifetime (Dimitrellos et al., 2020). Therefore, longwave cooling, the primary cause of turbulent overturning in stratocumulus (Wood, 2012), is not intensive enough to supply enough moisture for the cloud formation. Near cloud top, radiative cooling (Fig. 11f), apparently weaker than turbulent cooling, is usually balanced by the turbulent warming (Fig. 11e, f and h). In a few cases, the magnitude of radiative cooling is comparable to the turbulent cooling, but still can be offset by the turbulent warming, illustrated by Fig. 15d. As extreme turbulent cooling happens together with extreme longwave cooling (Fig. 15d), h_{lc} is mostly above the h_{tc} , while most h_{bw} (cloud top) is located below h_{tc} and overlapping with h_{bw} . This implies that, statistically, the cloud top is below the inversion and the longwave radiative cooling could be offset by the turbulent warming.

Below the cloud top there is always longwave warming, also apparently weaker than turbulent warming. In this case, thicker clouds usually develop with the existence of large-scale uplift, near the terminal

end of the WaMAI (Fig. 11a), where warm air converges with cold air. As thicker clouds formed, the turbulent-dominated energy pattern also diminishes in the boundary layer (Fig. 11e and h). Generally, in this category, turbulent heating is apparently larger than radiative heating and boundary layer warming is mostly contributed by turbulence (Table 4).

3.5. Radiation-dominated

Only around 26% of all WaMAIs belongs to category RAD (Table 3). For these, the large-scale subsidence is not as intensive as in category TBL (Table 4, CONV) and h_{tc} is also higher (Fig. 16a), suggesting that the stratocumulus develops more strongly (Table 4, TCLW; Fig. 16b), although cloud tops still remain constrained by the inversion (Fig. 12). At the cloud top, turbulent heat is distributed with warming below and cooling above, which implies entrainment mixing driven by longwave

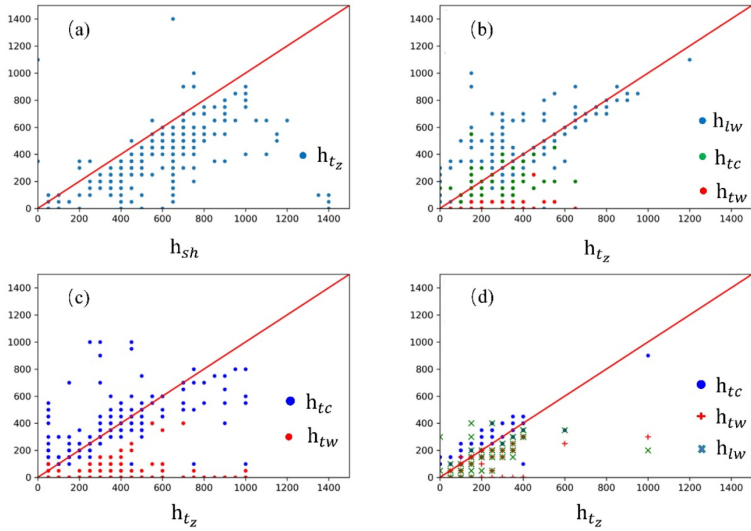


Fig. 15. Scatter plot showing the relative heights of different flux features on the boundary-layer heat budget: (a) the height to the maximum longwave heating (h_{sh}) against that to the maximum specific humidity (h_{tw}) for radiative-dominated WaMAIs, (b) h_{sh} , the height to the largest turbulence cooling (h_{tc}) and that to the largest turbulent warming (h_{tw}) against the height to the largest temperature gradient (h_{tc}) for radiative-dominated WaMAIs, (c) h_{tc} and h_{tw} against h_{tw} for turbulent-dominated WaMAIs, (d) h_{tc} , h_{tw} and h_{tw} against h_{tw} for turbulent-dominated WaMAIs with extreme longwave cooling (<-16 K/day). Red lines are the one-to-one line.

Table 3
Number of WaMAIs with boundary layer energy budget pattern of category TBL (turbulence-dominated), RAD (radiation-dominated), DIN (double inversion) and T&R (category TBL and RAD happen in one case).

Category	Kara	Laptev	East Siberian	Beaufort	Sum
TBL	32	45	32	35	144
RAD	5	17	22	17	61
DIN	0	1	2	1	4
T&R	5	1	8	15	29

radiation (Fig. 12h, 13h, highlighted with a rectangle). As this entrainment mixing provides the moisture for the cloud development from the warmer and moister air aloft, the TCLW is usually larger and hence the cloud top can emit more longwave radiation. This enhances the longwave cloud-top cooling and intensifies the cloud development (Moeng et al., 1996; Wood, 2012) and maintains the inversion. As this cloud formation process persists along the trajectories, more and more moisture from above the inversion is consumed and the cloud top is lifted, along the temperature and humidity inversions. With more cloud water produced than in category TBL, longwave radiative cooling is also partially balanced by the latent heat (Fig. 12g). The warming in the boundary layer is contributed by turbulent heat, latent heat, shortwave and longwave warming together (Fig. 12e, f and h). For this category, F_{lw} is much larger than that in category TBL, but all other surface energy-budget terms are smaller (Table 4). This can also be seen in a

Table 4
Averaged F_{sh} , F_{lh} , F_{sw} , F_{lw} , TCLW (from bottom to h_{tw} , $g\ m^{-2}$) and large-scale convergence (CONV; $10^{-5}\ kg\ m^{-2}\ s^{-1}$) from category TBL and category RAD.

	Category TBL	Category RAD
F_{sh}	43.0 \pm 81.2	8.77 \pm 12.1
F_{lh}	19.2 \pm 45.9	11.6 \pm 11.2
F_{sw}	-0.223 \pm 116	-4.16 \pm 63.3
F_{lw}	9.15 \pm 27.6	16.5 \pm 10.9
TCLW	17.2 \pm 44.4	82.7 \pm 50.8
CONV	94.1 \pm 173	30.9 \pm 83.5

Lagrangian perspective from 0 to 8 degrees north of the sea ice edge (Fig. 16c). However, farther north, F_{lw} and F_{sw} in category RAD is parallel to, while turbulent heat fluxes (F_{lh} ; $F_{lh} + F_{sh}$) is much smaller than, those in category TBL (Fig. 16c). Generally, F_{total} in category RAD is somewhat weaker than that in category TBL all the way to the central Arctic (Fig. 16d).

3.6. c. Decoupled inversions

The above discussed set of coupled mechanisms, where cloud formation and cloud top cooling along with turbulent transfer of heat strikes a balance, only works below the maximum of specific humidity; above this maximum, entrainment would bring drier air into the cloud-capped PBL and suppress the cloud development. That is why mostly h_{tw} is below h_{sh} (the height of maximum specific humidity) in Fig. 15a. In

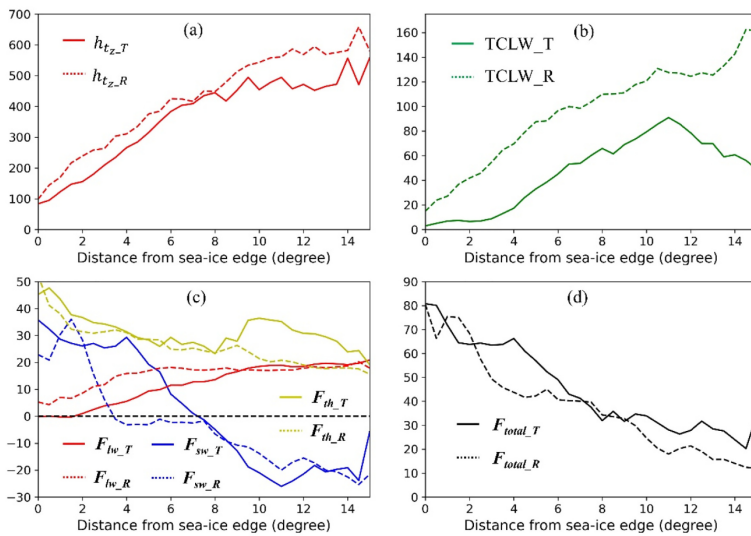


Fig. 16. Average anomalies of (a) the height to the maximum temperature gradient (m); (b) total column cloud liquid water from surface to h_u ($g\ m^{-2}$); (c) F_{hw} (blue), F_{th} (red) and surface turbulent heat flux (yellow; F_{th}); (d) surface net energy-budget from ERA5. In (a–d), solid lines represent variables from category TBL and dash lines represent category RAD.

very few cases, h_{th} is farther away from the initial inversion (Fig. 13d). The cloud top, in conjunction with the inversion, is lifted faster and gradually separates from the initial inversion; this forms a double inversion structure (Fig. 13c, Table 3 DIN). In the lower inversion, the energy budget is dominated by turbulent cooling (Fig. 13h), similar to category TBL, while in the upper inversion, energy budget of the boundary layer is dominated by longwave radiative cooling (Fig. 13f), similar to category RAD. Local observations indicate that decoupled cloud layers are common in the central Arctic (e.g. Brooks et al., 2017), while model evaluations indicate that the IFS has a problem describing the underlying physics (e.g. Sotiropoulou 2016). Hence the low frequency of occurrence of this case here should be interpreted with some caution.

In some cases, turbulent cooling is located right below the radiative cooling. The mechanism is similar to the double inversions, but the distance between the inversions is too small to be considered as double inversions. As mentioned earlier, the cloud top lies just beneath or in the maximum specific humidity. Since the maximum specific humidity in these cases is just a small distance above the upper edge of the inversion, the distance between the inversions maintained by radiative cooling and turbulent cooling, respectively, is too small to be detected from inspecting temperature contours, but can still be identified from the energy budget pattern. This energy pattern can be illustrated statistically by Fig. 15b. h_{hw} is located near or above h_{tc} , while h_{tc} lies right below h_{hw} with h_{hw} right at the bottom.

3.7. Transition between categories

In some cases, clouds beneath the inversion are very thin at the beginning of the trajectory but develops strongly after the warm air is advected over the sea ice for a considerable distance (Table 3 T&R,

Fig. 14). As the clouds are thin at the beginning, the energy budget in the boundary layer is turbulence-dominated (Fig. 14h, south of 80°N) belonging to category TBL, while after the clouds has developed, the energy budget pattern in the boundary layer becomes radiation-dominated (Fig. 14f, north of 80°N), belonging to category RAD.

4. Conclusion

In this study, we have detected WaMAIs over the sea sectors of Kara, Laptev, East Siberian and Beaufort in 40 recent summers (JJA from 1979 to 2018) using the ERA5 reanalysis. The climatological analysis shows that blocking high-pressure systems over corresponding sea sectors contribute to transport warm-and-moist air into summer Arctic on the western flank, supplying moisture for cloud formation. The cloud water exerts a positive total energy-budget anomaly on the surface ($11\text{--}18\ W\ m^{-2}$), contributed by positive anomalies in the longwave radiative heat flux ($5\text{--}8\ W\ m^{-2}$) and the turbulent heat fluxes (sensible and latent; $8\text{--}13\ W\ m^{-2}$), often moderated by a negative shortwave anomaly ($-9\text{--}+1\ W\ m^{-2}$). In comparison with CERES products, surface shortwave flux is $2\text{--}3\ W\ m^{-2}$ underestimated in ERA5 but surface longwave flux is $3\text{--}4\ W\ m^{-2}$ overestimated, which implies that ERA5 overestimates the amounts of clouds. However, the overall surface radiation flux from ERA5 is comparable with that from CERES.

We have also analysed the boundary-layer vertical structure and the associated energy-budget pattern of WaMAIs along their trajectories and find two main categories: turbulence-dominated (category TBL, Fig. 17a) and radiation-dominated (category RAD, Fig. 17b), comprised of 62% and 26% WaMAIs respectively. In response to less large-scale subsidence, stratocumulus develops more strongly in category RAD with 3 times more TCLW and hence exerts a $\sim 7\ W\ m^{-2}$ more intensive longwave flux on the surface and more intensive cloud-top cooling,

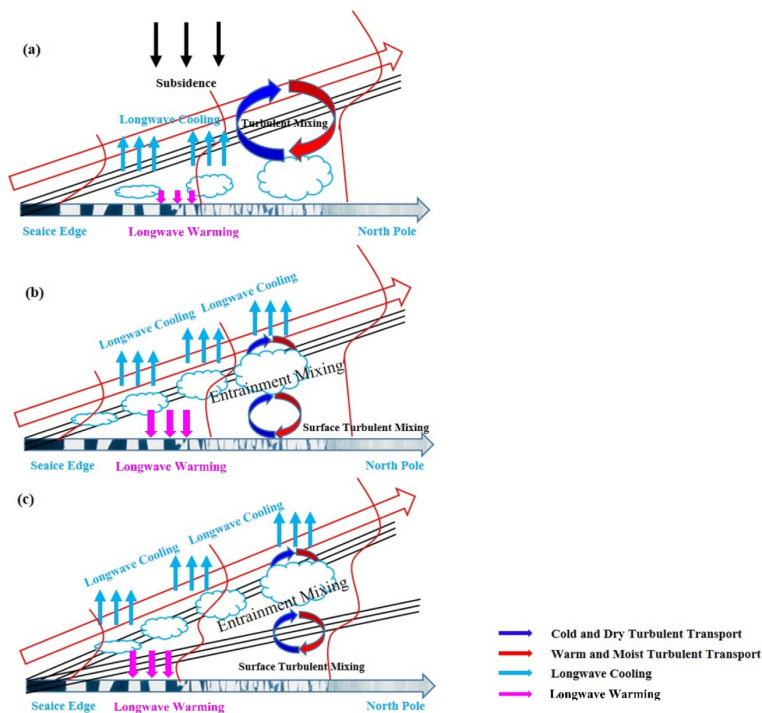


Fig. 17. Concept graph of turbulence-dominated WaMAI (a), radiation-dominated WaMAI (b), WaMAI with double inversions (c). The red lines in (a)(b)(c) are temperature or humidity profiles. Red arrows represent the WaMAIs. The horizontal arrows represent the Arctic surface with melting sea-ice. Black lines represent inversions.

while the heating/cooling due to sensible turbulent fluxes and surface shortwave flux are more than two times larger in category TBL. For most cases in category RAD, entrainment mixing at the cloud top is coupled with surface turbulent mixing. In category RAD, the maximum in specific humidity is located just above the inversion. However, if this maximum is located farther up from the temperature inversion, stratocumulus develops upward to the height of the maximum specific humidity. Entrainment and cloud-driven mixing at the cloud top then separates from the surface turbulent mixing (Fig. 17c). In this case, two inversion are formed; one above the original (cf. e.g. Brooks et al., 2017). In all categories, a well-mixed layer deepens gradually along the trajectory forced by continuous cloud-generated and surface-based turbulent mixing as was hypothesized in Tjernström et al. (2019b).

Statistically, as warm and moist air is advected over the sea-ice, the longwave flux anomaly increases linearly by $3 \text{ W m}^{-2} \text{ degree}^{-1}$ as the total column cloud liquid water increases linearly by $17 \text{ g m}^{-2} \text{ degree}^{-1}$, while north of 7 degrees, they continue the increase with a much lower rate. Meanwhile, the anomaly in shortwave flux decreases linearly as the cloud water increase linearly. However, the net cloud radiative effects are negative and the main contributor to the positive net surface energy-budget is turbulent heat flux.

Supplementary data to this article can be found online at <https://doi.org/10.1016/j.atmosres.2021.105586>.

[org/10.1016/j.atmosres.2021.105586](https://doi.org/10.1016/j.atmosres.2021.105586).

Declaration of Competing Interest

The authors declare that they have no known competing financial interests or personal relationships that could have appeared to influence the work reported in this paper.

Acknowledgements

This research was supported by the Swedish Research Council under Grant 2016-03807. The ERA5 data was downloaded from www.ecmwf.int/en/forecasts/datasets/reanalysis-datasets/era5, the AIRS data from <https://earthdata.nasa.gov/earth-observation-data/near-real-time/download-nrt-data/airs-nrt> and the CERES data from <https://ceres.larc.nasa.gov/data/>. The authors are grateful to Cian Woods for providing the trajectory calculation algorithm.

References

- Bowman, K.P., Lin, J.C., Stohl, A., Draxler, R., Konopka, P., Andrews, A., Brunner, D., 2013. Input data requirements for Lagrangian trajectory models. *Bull. Am. Meteorol. Soc.* 94, 1051–1058. <https://doi.org/10.1175/BAMS-D-12-00076.1>.

- Brooks, I.M., Tjernström, M., Persson, P.O.G., Shupe, M.D., Atkinson, R.A., Canut, G., Birch, C.E., Mauritsen, T., Sedlar, J., Brooks, I.M., 2017. The Turbulent Structure of the Arctic Summer Boundary Layer during the Arctic Summer Cloud-Ocean Study. *J. Geophys. Res. Atmos.* 122, 9685–9704. <https://doi.org/10.1002/2017JD027234>.
- Chahine, M.T., Pagano, T.S., Aumann, H.H., Atlas, R., Barnett, C., Blaisdell, J., Chen, L., Divakarila, M., Fetzer, E.J., Goldberg, M., Gautier, C., Granger, S., Hannon, S., Irlon, F.W., Kakar, R., Kalnay, E., Lambrigtsen, B.H., Lee, S.Y., Le Marshall, J., Mcmillan, W.W., Mcmillan, L., Olsen, E.T., Revercomb, H., Rosenkranz, P., Smith, W. L., Staelin, D., Strow, L.L., Susskind, J., Tobin, D., Wolf, W., Zhou, L., 2006. Improving weather forecasting and providing new data on greenhouse gases. *Bull. Am. Meteorol. Soc.* 87, 911–926. <https://doi.org/10.1175/BAMS-87-7-911>.
- Cohen, J., Screen, J.A., Furtado, J.C., Barlow, M., Whitleston, D., Comou, D., Francis, J., Deshoeff, K., Entekhabi, D., Overland, J., Jones, J., 2014. Recent Arctic amplification and extreme mid-latitude weather. *Nat. Geosci.* <https://doi.org/10.1038/ngeo2234>.
- Cox, C.J., Stone, R.S., Douglas, D.C., Stanitski, D.M., Gallagher, M.R., 2019. The Aleutian Low-Beaufort Sea Anticyclone: a climate Index Correlated with the timing of Springtime Melt in the Pacific Arctic Cryosphere. *Geophys. Res. Lett.* 46, 7464–7473. <https://doi.org/10.1029/2019GL083306>.
- De Boer, G., Shupe, M.D., Caldwell, P.M., Bauer, S.E., Persson, O., Boyle, J.S., Kelley, M., Klein, A., Tjernström, M., 2014. Near-surface meteorology during the Arctic Summer Cloud Ocean Study (ASCOOS): evaluation of reanalyses and global climate models. *Atmos. Chem. Phys.* 14, 427–445. <https://doi.org/10.5194/acp-14-427-2014>.
- Derksen, C., Brown, R., 2012. Spring snow cover extent reductions in the 2008–2012 period exceeding climate model projections. *Geophys. Res. Lett.* 39 <https://doi.org/10.1029/2012GL053387>.
- Devasthale, A., Sedlar, J., Kahn, B.H., Tjernström, M., Fetzer, E.J., Tian, B., Teixeira, J., Pagano, T.S., 2016. A decade of spaceborne observations of the arctic atmosphere novel insights from nasa's air instrument. *Bull. Am. Meteorol. Soc.* 97, 2163–2176. <https://doi.org/10.1175/BAMS-D-14-00202.1>.
- Dimitrellos, A., Ekman, A.M.L., Caballero, R., Savre, J., 2020. A sensitivity study of arctic air-mass transformation using large Eddy simulation. *J. Geophys. Res. Atmos.* 125 <https://doi.org/10.1029/2019JD031738>.
- Francis, J.A., Vavrus, S.J., 2012. Evidence linking Arctic amplification to extreme weather in mid-latitudes. *Geophys. Res. Lett.* 39 <https://doi.org/10.1029/2012GL051000>.
- Gong, T., Luo, D., 2017. Ural blocking as an amplifier of the Arctic Sea ice decline in winter. *J. Clim.* 30, 2639–2654. <https://doi.org/10.1175/JCLI-D-16-0548.1>.
- Gong, T., Feldstein, S., Lee, S., 2017. The role of downward infrared radiation in the recent arctic winter warming trend. *J. Clim.* 30, 4937–4949. <https://doi.org/10.1175/JCLI-D-16-0180.1>.
- Graham, R.M., Cohen, L., Ritzhaupt, N., Segger, B., Graversen, R.G., Rinke, A., Walden, V.P., Granskog, M.A., Hudson, S.R., 2019a. Evaluation of six atmospheric reanalyses over Arctic Sea ice from winter to early summer. *J. Clim.* 32, 4121–4143. <https://doi.org/10.1175/JCLI-D-18-0643.1>.
- Graham, R.M., Hudson, S.R., Mantrilli, M., 2019b. Improved Performance of ERA5 in Arctic Gateway Relative to four Global Atmospheric Reanalyses. *Geophys. Res. Lett.* 46, 6138–6147. <https://doi.org/10.1029/2019GL082781>.
- Graversen, R.G., Mauritsen, T., Tjernström, M., Källén, E., Svensson, G., 2008. Vertical structure of recent Arctic warming. *Nature* 451, 53–56. <https://doi.org/10.1038/nature06502>.
- Hersbach, H., Bell, B., Berrisford, P., Hirahara, S., Horányi, A., Muñoz-Sabater, J., Nicolas, J., Peubey, C., Radu, R., Schepers, D., Simmons, A., Soci, C., Abdalla, S., Abellan, X., Balsamo, G., Bechtold, P., Biavati, G., Bidlot, J., Bonavita, M., De Chiara, G., Dahlgren, P., Dee, D., Diamantakis, M., Dragani, R., Flemming, J., Forbes, R., Fuentes, M., Geer, A., Haimberger, L., Healy, S., Hogan, R.J., Hólm, E., Janisková, M., Keeley, S., Laloyaux, P., Lopez, P., Lupu, C., Radnoti, G., de Rosnay, P., Rozum, I., Vamborg, F., Villaume, S., Thépaut, J.N., 2020. The ERA5 global reanalysis. *Q. J. R. Meteorol. Soc.* 146, 1999–2049. <https://doi.org/10.1002/qj.3803>.
- Jakobson, E., Vihma, T., Palo, T., Jakobson, L., Keernik, H., Jaagus, J., 2012. Validation of atmospheric reanalyses over the Central Arctic Ocean. *Geophys. Res. Lett.* 39 <https://doi.org/10.1029/2012GL051591>.
- Johansson, E., Devasthale, A., Tjernström, M., Ekman, A.M.L., L'Ecuyer, T., 2017. Response of the lower troposphere to moisture intrusions into the Arctic. *Geophys. Res. Lett.* 44, 2527–2536. <https://doi.org/10.1002/2017GL072687>.
- Kapsch, M.L., Graversen, R.G., Tjernström, M., 2013. Springtime atmospheric energy transport and the control of Arctic summer sea-ice extent. *Nat. Clim. Chang.* 3, 744–748. <https://doi.org/10.1038/nclimate1884>.
- Kapsch, M.L., Graversen, R.G., Tjernström, M., Bintanja, R., 2016. The effect of downwelling longwave and shortwave radiation on Arctic summer sea ice. *J. Clim.* 29, 1143–1159. <https://doi.org/10.1175/JCLI-D-15-0238.1>.
- Komatsu, K.K., Alexeev, V.A., Repina, I.A., Tachibana, Y., 2018. Poleward upgliding Siberian atmospheric rivers over sea ice heat up Arctic upper air. *Sci. Rep.* 8 <https://doi.org/10.1038/s41598-018-21159-6>.
- Lawrence, D.M., Slater, A.G., Tomas, R.A., Holland, M.M., Deser, C., 2008. Accelerated Arctic land warming and permafrost degradation during rapid sea ice loss. *Geophys. Res. Lett.* 35 <https://doi.org/10.1029/2008GL033985>.
- Lawrence, H., Bormann, N., Sandu, I., Day, J., Farnan, J., Bauer, P., 2019. Use and impact of Arctic observations in the ECMWF Numerical Weather Prediction system. *Q. J. R. Meteorol. Soc.* 145, 3432–3454. <https://doi.org/10.1002/qj.3628>.
- Liu, Y., Key, J.R., Vavrus, S., Woods, C., 2018. Time evolution of the cloud response to moisture intrusions into the Arctic during Winter. *J. Clim.* 31, 9389–9405. <https://doi.org/10.1175/JCLI-D-17-0896.1>.
- Messori, G., Woods, C., Caballero, R., 2018. On the drivers of wintertime temperature extremes in the high arctic. *J. Clim.* 31, 1597–1618. <https://doi.org/10.1175/JCLI-D-17-0386.1>.
- Moeng, C.H., Cotton, W.R., Bretherton, C., Chlond, A., Khairoutdinov, M., Krueger, S., Lewellen, W.S., MacVean, M.K., Pasquier, J.R.M., Rand, H.A., Siebesma, A.P., Stevens, B., Sykes, R.L., 1996. Simulation of a stratocumulus-topped planetary boundary layer: Intercomparison among different numerical codes. *Bull. Am. Meteorol. Soc.* 77, 261–278. [https://doi.org/10.1175/1520-0477\(1996\)077<0261:SOASTP>2.0.CO;2](https://doi.org/10.1175/1520-0477(1996)077<0261:SOASTP>2.0.CO;2).
- Naakka, T., Nygård, T., Vihma, T., Sedlar, J., Graversen, R., 2019. Atmospheric moisture transport between mid-latitudes and the Arctic: Regional, seasonal and vertical distributions. *Int. J. Climatol.* 39, 2862–2879. <https://doi.org/10.1002/joc.5988>.
- Overland, J.E., Wang, M., 2016. Recent extreme arctic temperatures are due to a split polar vortex. *J. Clim.* 29, 5609–5616. <https://doi.org/10.1175/JCLI-D-16-0320.1>.
- Pithan, F., Svensson, G., Caballero, R., Chechin, D., Cronin, T.W., Ekman, A.M.L., Neggers, R., Shupe, M.D., Solomon, A., Tjernström, M., Wendisch, M., 2018. Role of air-mass transformations in exchange between the Arctic and mid-latitudes. *Nat. Geosci.* <https://doi.org/10.1038/s41561-018-0234-1>.
- Rutan, D.A., Kato, S., Doelling, D.R., Rose, F.G., Nguyen, L.T., Caldwell, T.E., Loeb, N.G., 2015. CERES synoptic product: Methodology and validation of surface radiant flux. *J. Atmos. Ocean. Technol.* 32, 1121–1143. <https://doi.org/10.1175/JTECH-D-14-00165.1>.
- Sedlar, J., Tjernström, M., 2017. Clouds, warm air, and a climate cooling signal over the summer Arctic. *Geophys. Res. Lett.* 44, 1095–1103. <https://doi.org/10.1002/2016GL071959>.
- Serreze, M.C., Francis, J.A., 2006. The arctic amplification debate. *Clim. Chang.* 76, 241–264. <https://doi.org/10.1007/s10584-005-9017-y>.
- Simmonds, I., 2015. Comparing and contrasting the behaviour of Arctic and Antarctic Sea ice over the 35 year period 1979–2013. *Ann. Glaciol.* 56, 18–28. <https://doi.org/10.3189/2015aJoGloA909>.
- Sotiriopoulou, G., Sedlar, J., Tjernström, M., Shupe, M.D., Brooks, I.M., Persson, P.O.G., 2014. The thermodynamic structure of summer Arctic stratocumulus and the dynamic coupling to the surface. *Atmos. Chem. Phys.* 14, 12573–12592. <https://doi.org/10.5194/acp-14-12573-2014>.
- Sotiriopoulou, G., Sedlar, J., Forbes, R., Tjernström, M., 2016. Summer Arctic clouds in the ECMWF forecast model: an evaluation of cloud parametrization schemes. *Q. J. R. Meteorol. Soc.* 142, 387–400. <https://doi.org/10.1002/qj.2658>.
- Stengel, M., Schlundt, C., Stapelberg, S., Sus, O., Eliasson, S., Willén, U., Fokke Meinink, J., 2018. Comparing ERA-Interim clouds with satellite observations using a simplified satellite simulator. *Atmos. Chem. Phys.* 18, 17601–17614. <https://doi.org/10.5194/acp-18-17601-2018>.
- Susskind, J., Blaisdell, J.M., Iredell, L., 2014. Improved methodology for surface and atmospheric soundings, error estimates, and quality control procedures: the atmospheric infrared sounder science team version 6 retrieval algorithm. *J. Appl. Remote. Sens.* 8, 084994 <https://doi.org/10.1117/1.jrs.8.084994>.
- Tedesco, M., Fettweis, X., Mote, T., Wahr, J., Alexander, P., Box, J.E., Wouters, B., 2013. Evidence and analysis of 2012 Greenland records from spaceborne observations, a regional climate model and reanalysis data. *Cryosph.* 7, 615–630. <https://doi.org/10.5194/nc-7-615-2013>.
- Tjernström, M., Shupe, M.D., Brooks, I.M., Persson, P.O.G., Prytherch, J., Salisbury, D.J., Sedlar, J., Achtert, P., Brooks, B.J., Johnston, P.E., Sotiriopoulou, G., Wolfe, D., 2015. Warm-air advection, air mass transformation and fog causes rapid ice melt. *Geophys. Res. Lett.* 42, 5594–5602. <https://doi.org/10.1002/2015GL064373>.
- Tjernström, M., Pirazzini, R., Sandven, S., Sagen, H., Hamre, T., Ludvigsen, C., Beszczynska-Möller, A., Gustafsson, D., Heygster, G., Sejr, M., Ahlström, A., Navarro, P., Goekede, M., Zona, D., Buch, E., Johannessen, T., Sørensen, M., Soltwedel, T., Danielsen, F., 2019a. Synthesis of Gap Analysis and Exploitation of the Existing Arctic Observing Systems. <https://intaros.nersc.no/content/synthesis-gap-analysis-and-exploitation-existing-arctic-observing-systems>.
- Tjernström, M., Shupe, M.D., Brooks, I.M., Achtert, P., Prytherch, J., Sedlar, J., 2019b. Arctic summer airmass transformation, surface inversions, and the surface energy budget. *J. Clim.* 32, 769–789. <https://doi.org/10.1175/JCLI-D-18-0216.1>.
- Tjernström, M., Svensson, G., Magnusson, L., Brooks, I.M., Prytherch, J., Vüllers, J., Young, G., 2020. Central Arctic Weather forecasting: confronting the ECMWF IFS with observations from the Arctic Ocean 2018 expedition. *Q. J. R. Meteorol. Soc.* <https://doi.org/10.1002/qj.3971>.
- Vihma, T., Pirazzini, R., Fer, I., Renfrew, I.A., Sedlar, J., Tjernström, M., Lüpkes, C., Nygård, T., Notz, D., Weiss, J., Marsan, D., Cheng, B., Birnbaum, G., Gerland, S., Chechin, D., Gascard, J.C., 2014. Advances in understanding and parameterization of small-scale physical processes in the marine Arctic climate system: a review. *Atmos. Chem. Phys.* <https://doi.org/10.5194/acp-14-9403-2014>.
- Weissén, C., Tjernström, M., Bromwich, D.H., De Boer, G., Ekman, A.M.L., Bai, L.S., Wang, S.H., 2014. The Arctic summer atmosphere: an evaluation of reanalyses using ASCOS data. *Atmos. Chem. Phys.* 14, 2605–2624. <https://doi.org/10.5194/acp-14-2605-2014>.
- Wood, R., 2012. Stratocumulus clouds. *Mon. Weather Rev.* <https://doi.org/10.1175/MWR-D-11-00121.1>.
- Woods, C., Caballero, R., 2016. The role of moist intrusions in winter arctic warming and sea ice decline. *J. Clim.* 29, 4473–4485. <https://doi.org/10.1175/JCLI-D-15-0773.1>.
- Woods, C., Caballero, R., Svensson, G., 2013. Large-scale circulation associated with moisture intrusions into the Arctic during winter. *Geophys. Res. Lett.* 40, 4717–4721. <https://doi.org/10.1002/gl.50912>.
- You, C., Tjernström, M., Devasthale, A., 2020. Warm-air advection over melting sea-ice: a lagrangian case study. *Boundary-Layer Meteorol.* <https://doi.org/10.1007/s10546-020-00590-1>.